Modeling surface longwave radiation over high-relief terrain

Guangjian Yan[b], Zhong-Hu Jiao[a,b,*], Tianxing Wang[c], Xihan Mu[b]

[a] *State Key Laboratory of Earthquake Dynamics, Institute of Geology, China Earthquake Administration, Beijing 100029, China*
[b] *State Key Laboratory of Remote Sensing Science, Jointly Sponsored by Beijing Normal University and Institute of Remote Sensing and Digital Earth of Chinese Academy of Sciences, Beijing 100875, China*
[c] *Institute of Remote Sensing and Digital Earth, Chinese Academy of Sciences, Beijing 100101, China*

ABSTRACT

Thermal anisotropy is an important phenomenon in thermal infrared remote sensing as it restricts the retrieval accuracy of surface longwave radiation (SLR). Topography is an essential controlling factor for the directionality of SLR for high-relief regions (e.g., mountain regions) where there is land surface heterogeneity and non-isothermal properties at pixel scales. However, satellite sensors can only receive radiance from a specific surface object at a small number of simultaneous viewing angles, which makes the quantitative modeling of thermal anisotropy challenging. Therefore, we developed the topographic longwave radiation model (TLRM) to describe the directionality of SLR components taking into account the variability of both subpixel topography and thermal anisotropy in high-relief regions. The reliability of TLRM was validated using the Discrete Anisotropic Radiative Transfer (DART) model over two typical geomorphic areas: a valley scene and a peak scene. The preliminary validation shows good agreement in terms of surface upward longwave radiance, which confirms the potential of TLRM for capturing the anisotropic patterns of land surfaces. The radiance values simulated by the DART model were first revised for the spectral mismatch. Then, they are used to correct residual deviation for TLRM using linear regressions. The root mean square error (RMSE) and coefficient of determination (R^2) were 0.830 W/($m^2 \cdot sr$) and 0.746 for the valley scene, respectively, and 0.239 W/($m^2 \cdot sr$) and 0.711 for the peak scene, respectively. Compared with TLRM, models that do not consider terrain effects generate significant discrepancies in high relief SLR components. The differences in downward longwave radiation can reach -60 W/m^2 in valleys without considering terrain effects. Based on the reference of hemispherical upward longwave radiation, surface upward longwave radiation estimated by the direct estimation method had a bias of 11.41 W/m^2 and standard deviation (STD) of 7.30 W/m^2, while the directional upward longwave radiation had a bias of 5.99 W/m^2 and STD of 4.08 W/m^2, showing lower estimation variation. The discrepancy between surface net longwave radiation (NLR) and terrain-corrected NLR ranged between 50 and -130 W/m^2 with clear negative biases mainly occurring in valleys. With higher spatial resolutions of remotely sensed imagery, the influence of complex terrain on land surface radiative flux has become more significant. This parameterization scheme is expected to better represent the topographic effects on SLR, enhance understanding of thermal anisotropy in non-isothermal mixed pixel areas of high relief, and improve the inversion accuracy of SLR.

1. Introduction

Surface longwave radiation (SLR) is a critical component of the energy balance at the Earth's surface, and accurate retrieval of SLR using remote sensing data is required for many fields, including climatology, hydrology, and agriculture (Wang et al., 2018a; Wielicki et al., 1996). Currently, the most-commonly used thermal infrared (TIR) satellite imageries are those from the Moderate Resolution Imaging Spectroradiometer (MODIS) and the Visible Infrared Imaging Radiometer Suite (VIIRS), both of which have moderate spatial

resolutions (~1 km and 750 m, respectively). Hence, a pixel is usually a mixed pixel that includes various three-dimensional (3D) structures. Surface upward longwave radiation (SULR), and consequently land surface temperature (LST), derived from remotely sensed data are strongly anisotropic owing to many factors, including the spatial arrangement of different surface types (Kimes and Kirchner, 1983), soil properties (Labed and Stoll, 1991), and vegetation structures (Francois et al., 1997; Lagouarde et al., 1995; Ren et al., 2013a). Topography is a major cause of SLR anisotropy (Müller and Scherer, 2005; Yan et al., 2016), and studies have shown that at large scales, SLR anisotropy and

surface radiation balance are more affected by topography than by vegetation canopies (Lagouarde et al., 2004; Sugawara and Takamura, 2006) or other land surface processes (Liou et al., 2007).

Over the past three decades, only a small number of studies have focused on modeling SLR in areas of complex relief (e.g., mountain regions). These studies were always conducted within snow-covered mountainous areas such as the European Alps (Hock and Holmgren, 2005; Matzinger et al., 2003; Olyphant, 1986a,b) and focused on modeling the terrain impact on atmospheric thermal radiation, surface thermal emissions, and the adjacent terrain radiation. However, in recent years, studies have attempted to accurately model interactions among sensor-surface-atmospheres in mountainous regions in order to retrieve SLR (Yan et al., 2016).

For surface downward longwave radiation (SDLR) in complex terrains, Olyphant (1986a) indicated that the anisotropy of terrain radiation and atmospheric effects should be considered in topographic radiation models. For steep terrain in cold or very dry areas (e.g., the Tibetan Plateau, the Arctic, and the Antarctic), atmospheric downward longwave radiation is relatively small. Thus, the emitted radiation of the surrounding terrain becomes relatively more important and is the major source of the total SDLR (Sicart et al., 2006). Olyphant (1986b) analyzed SDLR in the European Alps and concluded that the surrounding terrain radiation can enhance SDLR and reduce the loss of approximately 50% of surface net longwave radiation (SNLR). Among different components, the reflected radiation of the surrounding terrain is very small because the reflectivity of the ground surface is very low. Moreover, the atmosphere absorbs longwave radiation that propagates between mountain slopes, which further complicates the calculation of SDLR.

The SULR in mountainous areas is more complex than the SDLR. It is strongly influenced by surface temperature, emissivity, and the terrain itself. Liu et al. (2006) analyzed the importance of terrain factors in the upscaling of LST. In mountain areas, the joint effects of satellite geometry and variable temperatures at the subpixel scale, can result in an LST error of > 9 K (Lipton and Ward, 1997); furthermore, it can affect the accuracy of the derived SULR. For heterogeneous scenes with a distinct 3D structure (such as urban regions), Fontanilles et al. (2008) proposed an aggregation model that takes into account the radiative contributions of 3D structures and their interactions. The results showed that environmental radiation can account for $> 10\%$ of the total radiation and that the radiative temperature difference can reach 10 K or more at different viewing angles. The simulation results for a complex scene present that the brightness temperature (BT) are significantly influenced by the viewing angle and by the temperature difference between subpixels (Fontanilles et al., 2010).

Although many studies of shortwave radiation have been published (e.g., Lai et al., 2010; Müller and Scherer, 2005; Wang et al., 2018b), SLR modeling with accurate consideration of terrain effects remains immature. A small number of studies have considered interactions between longwave radiation and complex relief. Current knowledge of SLR in areas of high relief cannot explain the mechanism and influence of longwave radiation on the energy balance. Liou et al. (2007) developed a 3D Monte Carlo photon-tracing model for inhomogeneous and irregular terrain to calculate SLR. Nevertheless, no physically based model is available for SLR modeling in areas of high relief. This inhibits the development of parameterization algorithms for accurately retrieving SLR components from remote sensing data. As such, longwave radiation transfer in mountainous areas remains a major challenge (Liou et al., 2007; Yi et al., 2012).

The directional emission of longwave radiation at the pixel scale must also be considered. Li et al. (1999a) presented an equivalent directional emissivity model for heterogeneous, non-isothermal complex terrain, considering the differences in the visible area of the ground

surface from different viewing angles, multiple scattering of each component, and the temperature difference. Yan et al. (2001) further applied this method to estimate broadband directional thermal infrared radiation. Owing to the complexity of thermal radiation, most models are highly complex and have many input parameters. Although these models can more accurately describe the directional characteristics of surface thermal radiation, they are not well adapted to remote sensing applications. However, the models of Li et al. (1999a) and Yan et al. (2001) have better operability and can be used for the inversion of satellite data in terms of surface parameters.

The inaccurate assumption of homogeneous and isothermal surfaces is frequently employed in existing studies. For large-scale climate models, the differences in surface-averaged values are only on the order of 1 W/m^2 for surfaces $> 50 \times 50$ km^2 (Liou et al., 2007). Therefore, either the terrain is neglected or simplified schemes are incorporated to downscale the SLR (Fiddes and Gruber, 2014; Manners et al., 2012; Senkova et al., 2007). When considering subpixel variations in the estimation of SLR, terrain effects on longwave radiation become significant at the Earth's surface (Lee et al., 2013; Müller and Scherer, 2005). At present, many inversion algorithms treat the land surface as a horizontal plane, neglecting the effects of terrain on SLR. Thus, the induced uncertainty can be very large considering that approximately 24% of the Earth's land surface is mountainous, and 33% of Eurasia is covered by mountains. For instance, the bias of SNLR can reach 70 W/m^2 for cold mountainous surfaces compared with flat surfaces (Liou et al., 2007).

For SLR products that require high spatial resolutions, the terrain effect on SLR retrieval must be considered and modeled, such as for 1-km MODIS data. At 1-km pixel scales, the interactions of longwave radiation components and the anisotropy of SLR caused by subpixel terrain (such as terrain roughness and temperature differences between sunlit and shaded slopes) are significant (Liou et al., 2007; Minnis et al., 2004). Furthermore, TIR sensors such as MODIS have wide-view zenith angle ranges ($\pm 65°$) but limited view angle sampling, which limits the possibility to exactly describe the angular effects of thermal emissions. In addition, differences in observed features are distinct between the perspective projections of whiskbroom sensors and the orthographic projection that we expect. The thermal emissions of high relief surfaces received at the sensor show clear directionality due to the variable footprint of the sensor's field of view. These features can enhance the directionality of SLR and increase the difficulty in estimating the SLR over complex terrain. Therefore, existing inversion models that assume that the observed surface is horizontal have not been adapted for complex relief.

This study focused on modeling directional and hemispherical outgoing longwave radiation at pixel scales based on the surface properties and terrain characteristics of subpixels. First, the topographic longwave radiation model (TLRM) was developed to quantify terrain effects and accurately estimate SLR components in mountainous terrain using Advanced Spaceborne Thermal Emission and Reflection Radiometer (ASTER) and MODIS data. The terrain-corrected SDLR and hemispherical upward longwave radiation (HULR) were modeled by combining a directional thermal model at a non-isothermal surface and the terrain effects on SLR. Then, the terrain-corrected net longwave radiation (TNLR) was estimated from the terrain-corrected downward longwave radiation (TDLR) and HULR. TLRM was compared with the Discrete Anisotropic Radiative Transfer (DART) model to estimate its robustness. Three components of SLR calculated by TLRM were compared with existing methods to demonstrate the terrain effects. Finally, the impact of the atmosphere on the calculation of longwave radiation from surrounding terrain (LRST) was also analyzed.
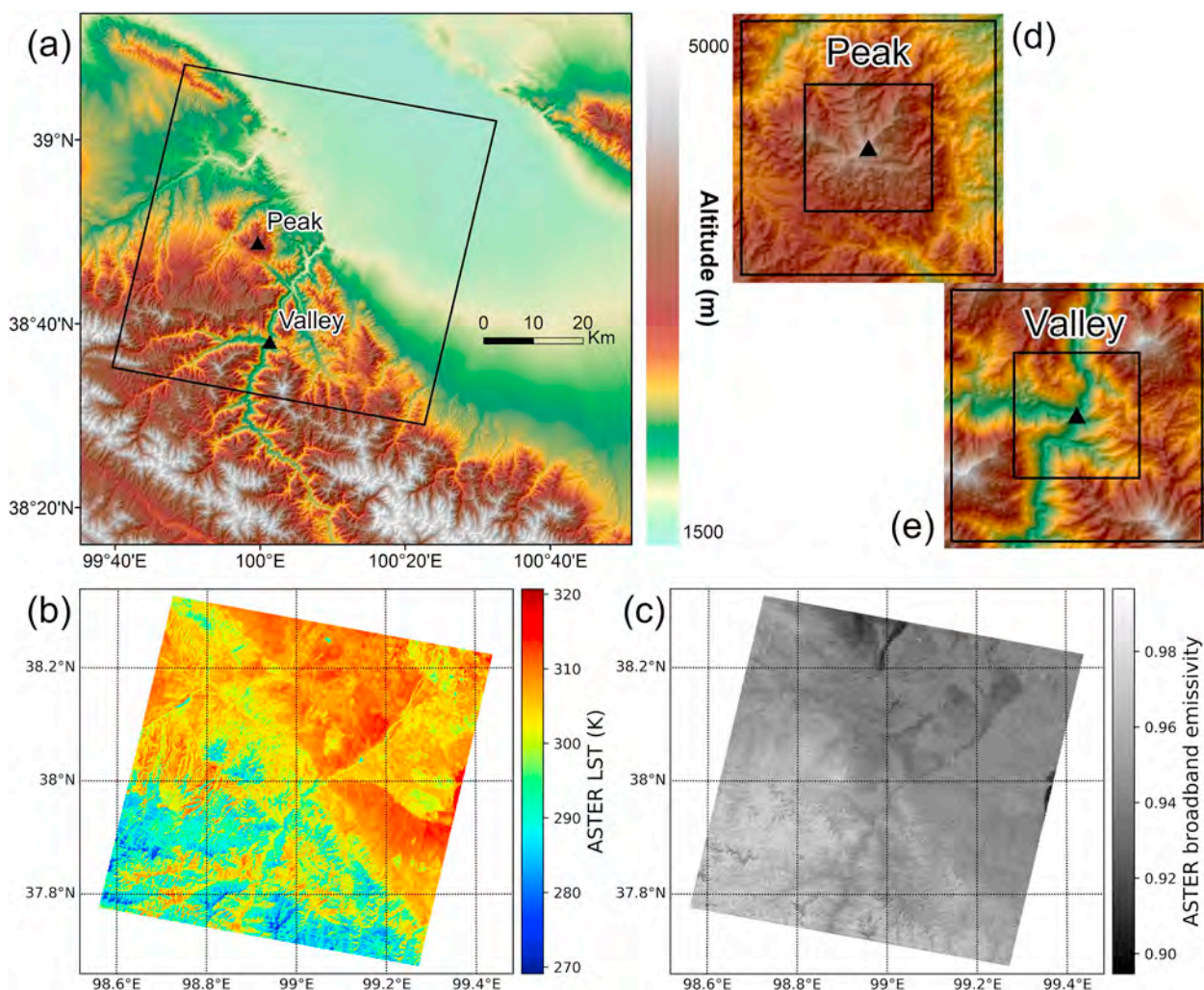
Fig. 1. Advanced Spaceborne Thermal Emission and Reflection Radiometer (ASTER) data for the study area. (a) ASTER topographic data at 30-m resolution; the black box denotes the coverage of ASTER land surface temperature (LST) and broadband emissivity. (b) ASTER LST at 90-m resolution. (c) ASTER broadband emissivity at 90-m resolution. (d) Topographic maps of the peak and (e) valley from a partially enlarged figure (a). Black triangles denote the central point of the representative area; the black square boxes cover areas of 5×5 km^2 and 10×10 km^2.

2. Study area and data

2.1. Heihe watershed

The study area (99°40′E − 100°33′E, 38°28′ N − 39°7′) is located at the upstream region of the Heihe River Basin, Gansu Province, China; this area is located within the Qilian Mountains, near the northeastern edge of the Tibetan Plateau. The major land cover types include bare land, grassland, farmland, forests, and water bodies. The study area contains both plains and mountains in an approximately 50:50 split (Fig. 1a). The mountains have highly variable topographical features that will clearly affect surface heterogeneity and thermal fluxes. This region serves as a good study area to demonstrate the impact of topography on SLR as the estimated longwave radiation of the plain area provides a useful reference.

2.2. Datasets

2.2.1. ASTER LST

ASTER is one of five instruments aboard the Terra satellite. It has

three optical systems, including five thermal infrared channels whose spatial resolution is 90 m and spectral range is 8–12 μm. The AST_08 data are an ASTER Level 2 surface temperature product with 90-m spatial resolution in the Universal Transverse Mercator (UTM) projection. This product is derived by a Temperature-Emissivity Separation (TES) algorithm based on five thermal infrared bands (AST09_T data: surface outgoing radiance after atmospheric correction) (Gillespie et al., 1998) with an accuracy of ± 1.5 K (Sobrino et al., 2007). The acquisition time of the ASTER image used in this study was 04:19:31 UTC on 3 May 2008. The central latitude and longitude of the image were 38.53°N and 100.25°E, corresponding to a solar zenith angle of 26.19° and azimuth angle of 147.89° at the time of the ASTER overpass. ASTER LST data are illustrated in Fig. 1b and range from approximately 270 to 320 K. LST changes caused by terrain are particularly evident between shadowed and sunlit slopes and for valleys and peaks.

2.2.2. ASTER broadband emissivity

In theory, the calculation of surface radiation balance requires broadband emissivity (BBE) for the entire spectral range; however, current remote sensing sensors can only provide narrow band
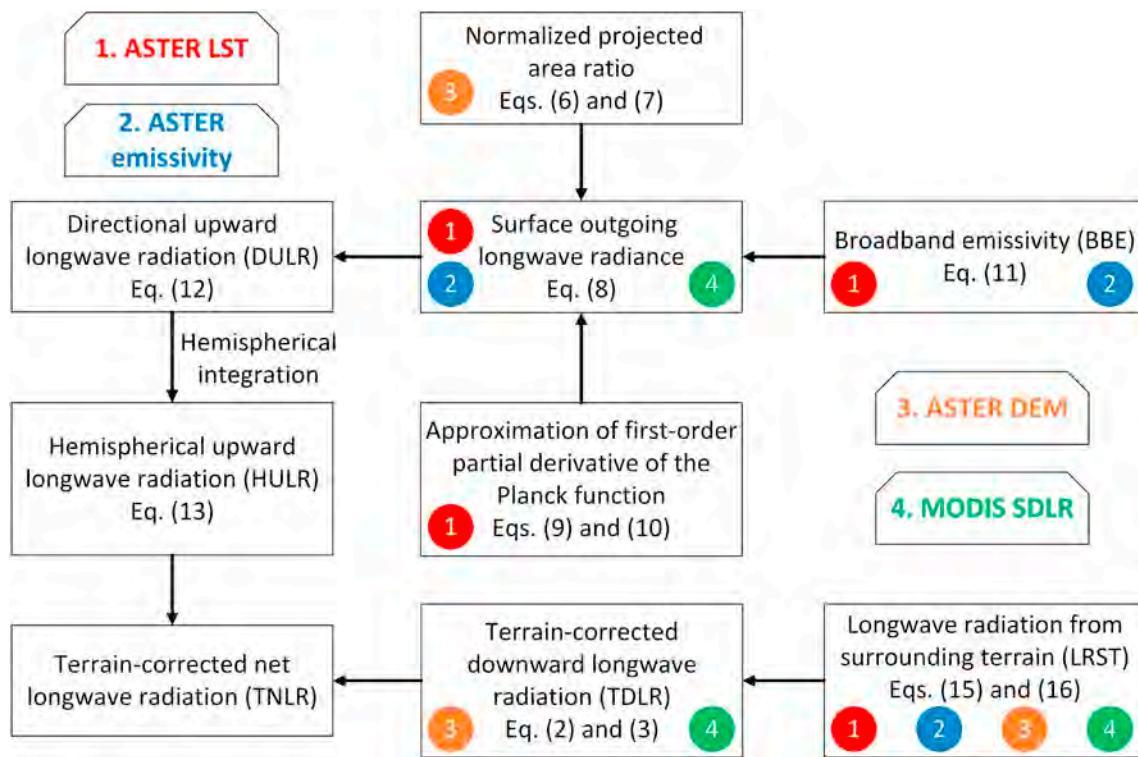
Fig. 2. Flowchart of the topographic longwave radiation model (TLRM) indicating the input and output data and the primary relationships among equations. Colored circles denote corresponding satellite data inputs. (For interpretation of the references to color in this figure legend, the reader is referred to the web version of this article.)

emissivity products in the range of 3 to 14 μm. Broadband emissivity in the range of 8–13.5 μm is believed to be optimal for the estimation of SNLR (Ogawa and Schmugge, 2004). Moreover, the impact of spectral emissivity above 14 μm on BBE is not significant (Ogawa et al., 2002). Therefore, we retrieved BBE from the ASTER narrowband emissivity product as the approximate value. The ASTER BBE in the 8–13.5 μm range was calculated using the following linear formula (Ren et al., 2013b):

$$\varepsilon_{8-13.5\mu m} = 0.088\varepsilon_{10} + 0.053\varepsilon_{11} + 0.174\varepsilon_{12} + 0.38\varepsilon_{13} + 0.305\varepsilon_{14} \qquad (1)$$

where ε_i is the ASTER band averaged emissivity (AST_05) containing five bands with 90-m spatial resolution (Gillespie et al., 1998). As shown in Fig. 1c, BBE is between 0.9 and 0.99 and some stripe noise caused by the sensor itself can be found. In general, the BBE is > 0.87, and is usually > 0.95 (Ogawa et al., 2003). To match the spatial resolutions of different products, ASTER emissivity and LST data were resampled using the cube convolution method to 30 m, the same resolution as the digital elevation model (DEM) data.

2.2.3. MODIS SDLR

MODIS is a key instrument aboard both of the two polar orbiting satellites, Terra (beginning from 18 December 1999) and Aqua (beginning from 4 May 2002). Its swath is approximately 2330 km and any position on the surface of the Earth can be viewed at least once or twice a day by each instrument (Barnes et al., 1998). The MODIS sensor has 36 channels between 0.405 and 14.385 μm. Multispectral thermal infrared data provide the potential for SLR retrieval. In addition, many widely verified standard MODIS land and atmosphere products represent high-quality data sources that are widely used by the remote-sensing community and can help to avoid errors caused by the use of

different sensor data products in the retrieval procedure.

The SDLR for a flat surface was retrieved from MODIS top-of-atmosphere radiance using the method of Wang et al. (2012). The acquisition times of MODIS and ASTER data were < 4 min apart. The SDLR retrieved for the plain region was higher than that for the mountainous areas. One reason for this is that the altitude of the mountains (up to > 4 km) is much higher than that of the plain (~1.5 km). The air temperature and LST of mountains are usually lower than those of plains, especially at the peaks, and thus the SDLR is correspondingly less. In flat farmland areas, vegetation canopies are denser; hence, air temperature and LST are lower than those of the surrounding desert or bare land, resulting in differences in SDLR.

2.2.4. Topographic data

DEMs provide basic data for describing the relief features of the land surface and can be used to calculate a number of variables, including slope, aspect, and sky view factor (SVF). Terrain data were collected from the 30-m ASTER GDEM (Global Digital Elevation Model) version 2.0, which was released in October 2011. GDEM v2 has absolute vertical and horizontal accuracies of 17 and 30 m, respectively (Tachikawa et al., 2011). The elevation of the study area is shown in Fig. 1a. The study area is dominated by high relief, especially in the southwest, with a relatively flat region found in the northeast; the topographic range is large (from approximately 1500 to 4700 m).

3. Modeling topographic longwave radiation components

The directionality of SLR is closely related to surface temperature and to the emissivity and 3D structure of the natural surface. However, it is challenging to estimate SLR for nonhomogeneous pixels from
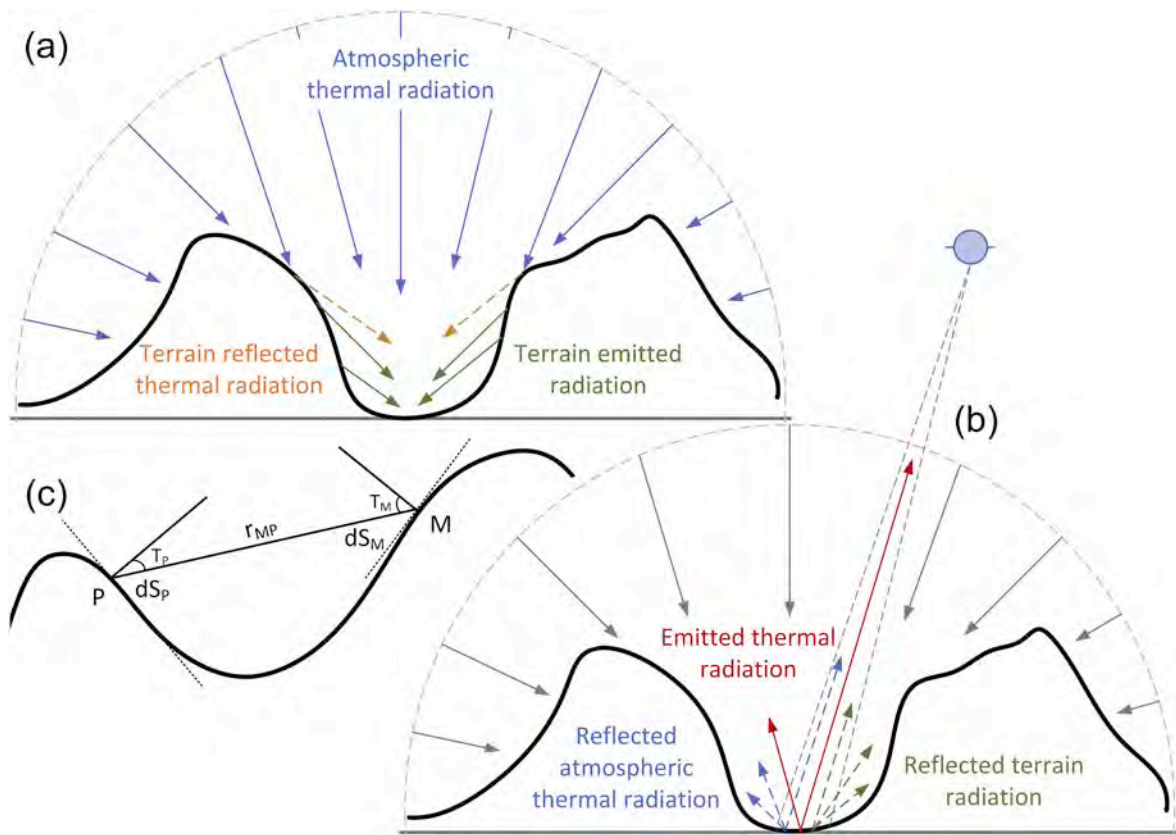
Fig. 3. Diagrams of modeling longwave radiation in areas of high relief. (a) Surface downward longwave radiation (SDLR) in mountainous terrain, including atmospheric thermal radiation, reflected terrain radiation, and emitted thermal radiation. (b) Surface upward longwave radiation (SULR) in mountainous terrain, including emitted thermal radiation, reflected atmospheric thermal, and terrain radiation components. (c) Calculation of longwave radiation from the surrounding terrain.

remote sensing data if all the possible affecting factors are considered. For this reason, only important parameters are modeled; secondary factors must be reasonably approximated or simplified. Among them, terrain is a significant factor when retrieving SLR with spatial resolution that is higher than those of reanalysis data products, whose spatial resolutions are always > 50 km (Senkova et al., 2007). Therefore, we focused on modeling SLR considering the subpixel terrain and thermal anisotropy caused by terrain effects.

Surface temperature and emissivity at subpixel scales are the dominant factors that control SLR, but these cannot be estimated directly from MODIS data. For this reason, ASTER LST and emissivity products at 90-m resolution were used for subpixel information. As ASTER and MODIS can quasi-synchronously acquire ground surface images, the advantage of this approach is that it is closer to the true ground state; however, the disadvantage is that it can only calculate SLR in the overlapping regions of two data sources. This study assumed subpixels with 30-m resolution within a 1-km MODIS pixel. Each subpixel was assumed to be Lambertian and at thermodynamic equilibrium, and each with a unique surface temperature and emissivity. Therefore, each subpixel followed Planck's law and Kirchhoff's law. Nevertheless, as a whole, each 1-km pixel was heterogeneous, non-isothermal, and exhibited anisotropic characteristics. In this situation, Planck's law and Kirchhoff's law are no longer valid and present the scale effect (Li and Wang, 1999; Li et al., 1999b). Consequently, a model designed to retrieve SLR components should correct this effect (Fig. 2).

3.1. Downward longwave radiation over high relief terrain

In the mountains, SDLR is generally anisotropic owing to three factors: 1) the influence of shadowing by adjacent terrain, which generally decreases SDLR; 2) the contribution of longwave radiation from surrounding terrain, which can increase SDLR; and 3) the anisotropy of atmospheric downward thermal emissions. The combined effects of these three factors make the estimation of SDLR in mountainous areas very complex. Under clear-sky conditions, the anisotropy of atmospheric radiation is generally not considered because its accurate estimation is very difficult. Moreover, the anisotropy of SDLR caused by topographic factors is more significant (Plüss and Ohmura, 1997). In the presence of topography, in addition to the atmosphere, LRST contributes to SDLR (Fig. 3a), and the impact on SDLR is significant and complex (Manners et al., 2012; Matzinger et al., 2003; Plüss and Ohmura, 1997).

Under the assumptions of a plane-parallel atmosphere, Lambertian surface, and thermodynamic equilibrium state, the SDLR (W/m^2) on a sloped surface that includes atmospheric thermal radiation ($E_0^\downarrow$) on a horizontal surface and emitted and reflected radiation from the adjacent terrain (E_T) is:

$$E^\downarrow = E_0^\downarrow V_d + E_T \qquad (2)$$

where V_d is the SVF calculated from ASTER DEM data, and $E_0^\downarrow$ is retrieved from MODIS data (see Section 2.2.3). The SVF is an essential surface geometry parameter in modeling surface radiation balance, and

is defined as the non-shadowed proportion of the hemisphere from the target point to the sky (Dozier and Frew, 1990; Jiao et al., 2019a). In this study, the definition of SVF was based on the slope coordinate system (Lai et al., 2010; Manners et al., 2012).

The problem of mixed pixels is inevitable when retrieving SLR. For a large remote sensing pixel (e.g., 1 km), we can assume that the SDLR is distributed uniformly in the subpixels without the influence of air turbulence and that the local state of energy balance is maintained. Considering the effect of the micro-slope of a subpixel on SDLR, the SDLR at the pixel scale is aggregated using the radiation of the subpixels based on the surface radiation balance:

$$E^{\downarrow} = \frac{\sum_i^N (E_0^{\downarrow} V_{d,i} + E_{T,i}) \sec \alpha_i}{\sum_i^N \sec \alpha_i} \tag{3}$$

where N is the number of subpixels within the pixel scale, and α is the slope angle of a subpixel derived from ASTER DEM data.

3.2. Directional upward longwave radiation

Spatial variations of SULR in mountainous areas are generally more complex than those of SDLR. The interaction between the observation geometry, 3D topography, and local surface temperature and emissivity enhances SULR anisotropy. The sensor (e.g., MODIS) can only acquire surface-leaving radiance from a single direction, including surface emitted radiation and reflection of both atmospheric radiation and radiation from the surrounding terrain (Fig. 3b). Elevation, terrain configurations, mountain shading, and shadow can produce very strong local radiation gradients that cause significant thermal anisotropy.

For directional thermal radiation at the pixel scale, which is characterized by non-isothermal heterogeneous components in a 3D structure, Li et al. (1999a) proposed a conceptual model for effective directional emissivity. This model assumes that the pixel has significantly different components, and that the directionality consists of directional thermal radiation of an isothermal rough surface and radiative increments due to the differences among LSTs. It is assumed that LST at the pixel scale does not change with observation direction, and that the directionality of surface land-leaving radiance is mainly caused by the anisotropy of surface effective emissivity. The total effective emissivity should also include the contribution of multiple scattering between components. Based on this model, we added the contribution of reflected SDLR and considered the variance in longwave radiation at different azimuth angles. The surface outgoing longwave radiance is expressed as follows:

$$L_\lambda(\theta, \varphi, T_0) = B_\lambda(T_0) \sum_i^N \Lambda_i(\theta\varphi)\varepsilon_{\lambda i} + L_\lambda^{\downarrow} \sum_i^N \Lambda_i(\theta\varphi)(1 - \varepsilon_{\lambda i}) + \frac{\partial B_\lambda(T_0)}{\partial T_0} \sum_i^N \Lambda_i(\theta\varphi)\varepsilon_{\lambda i} \Delta T_i \tag{4}$$

where θ is the view zenith angle (VZA); φ is the view azimuth angle (VAA); $L_\lambda^{\downarrow}$ is the SDLR at wavelength λ; $B_\lambda(T_0)$ is the Planck function; and ε_λ is the spectral emissivity. T_0 is the reference temperature of the pixel and is insensitive to the directional radiance. It is defined as the average LST of all visible subpixels from ASTER LST data (Li et al., 1999a; Yan et al., 2001).

The ΔT_i is the difference between the LST of a subpixel and T_0. The first-order partial derivative of the Planck function is:

$$\frac{\partial B_\lambda(T_0)}{\partial T_0} = \frac{C_1 C_2 \lambda^{-6} e^{C_2/(T_0\lambda)}}{T_0^2 (e^{C_2/(T_0\lambda)} - 1)^2} \tag{5}$$

where $C_1 = 1.191 \times 10^8$ and $C_2 = 1.439 \times 10^4$. The subpixel contributes different radiance values for different view directions owing to the existence of terrain that may obstruct the subpixel, causing it to be invisible to the sensor and that changes the projected area of the subpixel at the sensor level. These effects are expressed by the normalized projected area ratio $\Lambda(\theta, \varphi)$:

$$\Lambda_i(\theta, \varphi) = \frac{\Theta_i(\theta, \varphi)\cos\gamma_i \sec\alpha_i}{\sum_{j=1}^N \Theta_j(\theta, \varphi)\cos\gamma_j \sec\alpha_j} \tag{6}$$

and

$$\cos\gamma = \cos\alpha\cos\theta + \sin\alpha\sin\theta \cos(\varphi - \beta) \tag{7}$$

where γ is the relative VZA; β is the aspect angle of a tilted surface; and $\Theta(\theta, \varphi)$ is the terrain shadowing factor, which is set to one for pixels that are totally visible to the sensor, and zero otherwise. Eq. (4) includes three terms on the right-hand side: 1) direct emission of the surface, considering the surface heterogeneity; 2) reflection of SDLR containing multiple scattering radiations of the atmosphere and surrounding terrain; and 3) radiance change caused by different LST distributions at subpixel scales and directional emissivity due to 3D structures of the ground surface (Li et al., 1999a; Yan et al., 2001).

The next step is to convert the monochromatic radiance of Eq. (4) to broadband flux in the range of 4 to 100 μm (Jiao et al., 2015). For a narrowband sensor, the radiance at a central wavelength is always used to approximate the average radiance of a band. However, the retrieval of surface radiation balance requires broadband longwave radiation. Therefore, an efficient broadband thermal radiation model derived from Eq. (4) is proposed in order to reduce error from this approximation, to reduce the integration time, and thus to produce an operational remote sensing inversion method. The integrated equation for the longwave spectral range from λ_1 to λ_2 is as follows:

$$L_{\Delta\lambda}(\theta, \varphi, T_0) = \int_{\lambda_1}^{\lambda_2} L_\lambda(\theta, \varphi, T_0)d\lambda \approx \frac{\sigma T_0^4}{\pi} \sum_i^N \Lambda_i(\theta\varphi)\varepsilon_{bb,i}$$
$$+ L^{\downarrow} \sum_i^N \Lambda_i(\theta\varphi)(1 - \varepsilon_{bb,i}) + F_{\Delta\lambda}(T_0) \sum_i^N \Lambda_i(\theta\varphi)\varepsilon_{bb,i} \Delta T_i \tag{8}$$

where $L^{\downarrow}$ is the MODIS SDLR already corrected for topographic effects (see Section 3.1) and $F_{\Delta\lambda}(T)$ is approximated according to the method of Yan et al. (2001):

$$F_{\Delta\lambda}(T) = \int_{\lambda_1}^{\lambda_2} \frac{\partial B_\lambda(T_0)}{\partial T_0}d\lambda \approx \frac{C_1}{T}\left(\frac{\lambda^{-4}}{e^{\frac{C_2}{T\lambda}} - 1}\right)\Bigg|_{\lambda_1}^{\lambda_2} + B_{\Delta\lambda}(T) \tag{9}$$

and

$$B_{\Delta\lambda}(T) = \int_{\lambda_1}^{\lambda_2} B_\lambda(T)d\lambda$$
$$= \sum_i^n \frac{C_1 T}{iC_2 \lambda^3} \frac{1}{e^{iC_2/(T\lambda)}}\left(1 + 3\left(\frac{T}{iC_2}\lambda\right) + 6\left(\frac{T}{iC_2}\lambda\right)^2 + 6\left(\frac{T}{iC_2}\lambda\right)^2\right)\Bigg|_{\lambda_1}^{\lambda_2} \tag{10}$$

where n is the first n terms of polynomials for the approximation where $n = 12$ was used to calculate the broadband radiance; and ε_{bb} is BBE that is independent of the surface temperature (see Section 2.2.2). The variance of the surface emissivity is < 0.5% for temperatures between 270 and 330 K (Ogawa et al., 2002). Thus, ε_{bb} is the weighted average value using the Planck function of the reference temperature T_0:

$$\varepsilon_{bb} = \frac{\int_0^{\infty} \varepsilon_\lambda B_\lambda(T_0)d\lambda}{\int_0^{\infty} B_\lambda(T_0)d\lambda}. \tag{11}$$

The BBE $\varepsilon_{bb, i}$ and temperature difference ΔT_i are derived from ASTER narrowband emissivity and LST products (see Section 2.2). Under the assumption of isotropic radiance for a Lambertian surface, the conventional approach used in most retrieval methods without considering terrain effects is as follows:

$$E^{\uparrow} = \pi L_{\Delta\lambda}(\theta, \varphi, T_0). \tag{12}$$

3.3. Hemispherical upward longwave radiation

In complex terrain, the longwave radiation received by an inclined surface from the atmosphere and surrounding terrain is variable, and the surface-leaving thermal radiation of the slope is blocked by surrounding terrain; thus, only a proportion of this radiation can leave the land surface. Therefore, the observed radiance from different perspectives shows distinct anisotropy at the pixel scale, which can be derived from Eq. (12). To improve the retrieval accuracy of SULR, angular effects in both zenith and azimuth directions in hemispherical space should be considered. Directional thermal radiation modeling is thereby the basis for retrieving the HULR from the Earth's surface.

HULR is the integrated upward longwave radiation $L_{\Delta\lambda}(\theta, \varphi, T_0)$ in hemispherical space at the pixel scale, as shown in Eq. (13). It includes emitted thermal radiation, reflected SDLR, and incoming adjacent terrain radiation, among which the emitted thermal radiation is the main component. HULR can be deemed as the 'true' outgoing surface longwave radiation of a pixel and can better depict the characteristics of SULR in topographic regions.

$$E_H^\uparrow = \int_0^{2\pi} \int_0^{\pi/2} L_{\Delta\lambda}(\theta, \varphi, T_0) cos\theta sin\theta d\theta d\varphi. \tag{13}$$

For the numerical integration of this equation, a discretization scheme is used as follows:

$$E_H^\uparrow = \int_0^{2\pi} d\varphi \int_0^1 L_{\Delta\lambda}(\mu, \varphi, T_0)\mu d\mu \approx \Delta\mu \bullet \Delta\varphi \sum_N \sum_M L_{\Delta\lambda}(\mu, \varphi, T_0)\mu_N \tag{14}$$

where μ is the cosine of VZA; $\Delta\mu$ and $\Delta\varphi$ are the bins of μ and VAA, respectively; $N = 1/\Delta\mu$ and $M = 2\pi/\Delta\varphi$; and μ_N is the VZA after discretization. Intervals of VZA and VAA clearly have an effect on the integral results. Through a comparison of the numerical and analytical solutions, the combination of (20, 36) can be considered to achieve the optimal tradeoff between accuracy of the approximation calculation and computation time as indicated by Voogt (2008).

3.4. Longwave radiation from surrounding terrain

The LRST contributes an obvious amount to the target point in mountainous areas, especially in valleys. LRST includes the emission of sloped surfaces, reflection of atmospheric downward radiation, and multiple scattering of radiation among the atmosphere and surroundings. In most cases, the reflected radiation from surrounding terrain is small, and can thus sometimes be ignored (Gratton et al., 1993). However, when the downward emission from the atmosphere is small (e.g., cold and dry air in high altitude areas), LRST becomes more important (Sicart et al., 2006). In some basins covered by snow or ice, LRST accounts for approximately 20% of the total incident longwave radiation on clear days (Gratton et al., 1993) because surface emissivity is always higher than the clear-sky emissivity. On sunny days, when SVF is small (e.g., for a deep valley) and the surface temperature of the surrounding terrain is high, LRST can also reach a high value compared with the general scene.

Olyphant (1986b) showed that it is a problem to treat LRST as isotropic radiation. Moreover, multiple scattering plays an important role in the directionality of surface thermal radiation. In order to calculate this radiation more accurately, a pixel-by-pixel method capable of modeling multiple scattering effects of SLR was proposed by Proy et al. (1989). This approach considers the contribution of neighboring pixels to the target pixel by aggregating incident radiance of all visible pixels. The LRST received by slope M is (Fig. 3c):

$$E_{T,M} = \sum_{P=1}^N \frac{L_{adj} \cos T_M \cos T_P dS_P}{r_{MP}^2} \tag{15}$$

where N is the number of pixels that can be seen by point M; T_M and T_P are the angles of point M and P between the normal vector of the slope and the line MP, respectively; dS_P is the slope area of point P; and r_{MP} is the distance between points M and P. Here, the ASTER DEM data were used to calculate these angles in surface geometry. L_{adj} is the surface-leaving radiance of point P, including the thermal emission, downward longwave radiation ($E_P^\downarrow$) and radiation from surrounding terrain E_T:

$$L_{adj} = \frac{\Theta_{M\to P}}{\pi}[\varepsilon_P \sigma T_P^4 + (1 - \varepsilon_P)(E_P^\downarrow + E_T)] \tag{16}$$

where $\Theta_{M\to P}$ is the shadowing factor from point M to point P; ε_P is the ASTER BBE of point P; and σ is the Stefan-Boltzmann constant ($5.6697 \times 10^{-8}Wm^{-2}K^{-4}$).

Note that there is a mutual dependence between Eq. (15) and Eq. (16) because of the E_T term. To solve this problem, E_T in L_{adj} is neglected in the first iteration, and then the calculated E_T is used in the second iteration to complete the final calculation of E_T. At the same time, the change in longwave radiation caused by the thermal emission and atmospheric absorption between two visible pixels is not considered in Eq. (16); this is further discussed in Section 5.3.

4. DART simulation for model comparison

Owing to the influence of local terrain, the representativeness of measured longwave radiation data in mountainous areas is always insufficient at the pixel scale (Hoch and Whiteman, 2010; Matzinger et al., 2003). There remains a lack of available datasets that can be used to effectively explore the terrain effects on SLR; furthermore, methods to quantitatively model such effects are rarely available. Therefore, quantitative validation between TLRM and ground measurements in high relief regions is challenging. In this study, we compared the TLRM-derived surface upward longwave radiance with the radiance simulated by the DART model (Version 5.7.5 build 1141) to validate the rationality of the TLRM.

DART is a 3D radiative transfer model that offers an effective and highly accurate method for simulating complex 3D scenes associated with their SLR components (Gastellu-Etchegorry et al., 2015; Gastellu-Etchegorry et al., 1996). It provides effective tools for generating and importing different landscape configurations, including land cover types, atmospheric conditions, and topographical features. The DART model can thus simulate radiative transfer in 3D scenes such as urban and natural landscapes with vegetation, water bodies, clouds, buildings, topography, and atmosphere present. It tracks radiation fluxes within 3D landscapes by different simulation methods (e.g., ray-tracing, discrete ordinate, and Monte Carlo methods) and covers the reflective to emissive spectrums. The remotely sensed images of radiance and BT can be simulated for specific wavelengths, solar/viewing directions, spatial resolutions, and sensor types. The DART model has been successfully applied and validated against field measurements and remote sensing data (Sobrino et al., 2011) and is recognized as one of the most accurate 3D simulation models assessed by Radiation Transfer Model Intercomparison experiments (Widlowski et al., 2015).

Two representative geomorphic regions (a valley and a peak; Fig. 1d and e) were selected to demonstrate the results of the TLRM and DART models. As the DART model is complicated and computationally demanding, it is almost impossible to load each pixel in the study area as this would cause a severe slowdown in processing. Hence, we choose a small neighborhood size to be able to parameterize the DART model in an appropriate manner.

ASTER DEM, LST, and BBE data for the 165 × 165 pixels with a

Table 1

Discrete Anisotropic Radiative Transfer (DART) model input parameters for simulating the thermal images of valley and peak landscapes.

Catalog	Setting
Flux-tracking	Radiative method: Flux-tracking Atmosphere radiative transfer: Analytic model
Flux-tracking/advanced mode	Flux Tracking → Scene albedo/thermal exitance threshold: 0.001 Flux Tracking → Maximum number of scene crossed by a ray: 1000 Flux Tracking → Smaller mesh size D of BOA irradiance sources (m): 6 Flux Tracking → Factor N (N³ sub-cells per cell): 1 Flux Tracking → Subface subdivision S for thermal emission [m²]: 1.0
Flux-tracking/flux-tracking parameters	Atmosphere brightness temperature: 300 K Smaller mesh size D of BOA irradiance (m): 1.0 Spectral band: 60 bands in 8 to 14 μm Mode: Mode T Thermal emission law: Planck
Flux-tracking/products	BRF/BTF Products, Radiance products Maximal zenith angle of images: 89.0 OrthoImages and irradiance: Industry Standard
Direction input parameters	Sun angles or date: Viewing angle Sun zenith angle: 26.0 Sun azimuth angle: 147.85 Day of the year: 124
Direction input parameters/add single direction	720 angles
Optical and temperature properties	Lambertian and Temperature for each scene pixel
Earth scene	Exactly periodic scene: Infinite slope Whole or sub-Earth scene: Whole Cell dimensions → x and y [m]: 30.0 Cell dimensions → z [m]: 1.0 Earth scene dimensions: x and y [m]: 4950.0 Presence of Topography: Yes
Atmosphere	USSTD76 gas model Rural-23 km aerosol model

Fig. 4. Linear fitness for MODerate resolution atmospheric TRANsmission (MODTRAN) simulated radiance between spectral ranges of 4–100 μm and 8–14 μm. The red line is the linear regression line. (For interpretation of the references to color in this figure legend, the reader is referred to the web version of this article.)

MODerate resolution atmospheric TRANsmission (MODTRAN) as described by Jiao et al. (2015). MODTRAN is an atmospheric radiative transfer model used worldwide to simulate the process of radiative transfer through the atmosphere from the ultraviolet to the far infrared regions of the spectrum (Berk et al., 2006). Six built-in model atmospheres were used. The surface properties were described by 30 items of spectral emissivity data from the MODTRAN built-in emissivity database. The surface temperature ranged from 210 to 330 K with increments of 2 K. The concentration of carbon dioxide was 390 ppm and the rural aerosol model was used to indicate the type of extinction and the meteorological range of the boundary layer. The surface height was set from 1 to 5 km with a step of 500 m. The sensor looked vertically downward in the nadir direction.

The linear regression for MODTRAN simulated radiance values of 8–14 μm and 4–100 μm shows good performance (Fig. 4). The bias was almost zero and the root mean square error (RMSE) and coefficient of determination (R^2) were 1.46 W/($m^2 \cdot sr$) and 0.999, respectively. Consequently, a linear conversion ($R_{4-100\mu m} = 2.328 \cdot R_{8-14\mu m} + 18.726$) was established to eliminate radiance band differences, and the revised radiance derived from the DART model was used to compare with TLRM radiance.

5. Results and discussion

5.1. Preliminary validation using the DART model

The valley and peak scenes calculated by the TLRM and simulated by the DART model showed good consistency in terms of radiance values and angular distributions. Radiance ranged from approximately 138 to 148 W/($m^2 \cdot sr$) for the valley scene (Fig. 5a and b), and from approximately 127 to 130 W/($m^2 \cdot sr$) for the peak scene (Fig. 5d and e). The valley scene exhibited stronger variations and higher complexity of the angular characteristics of radiance than did the peak scene. The hotspot effect of radiance was in accordance with the solar position at the time of the ASTER overpass (black circle in Fig. 5a). The distribution of surface temperature in 3D space correlated with the direction of the sun, causing a phenomenon similar to the hotspot effect (Jiao et al.,

spatial resolution of 30 m around the two sites were used as the input for the DART model. ASTER DEM data were used as the topography of 'Earth scene'. ASTER LST data were imported into 'Optical and Temperature properties' for each pixel temperature. The Lambertian attribute of "Optical and Temperature properties" was obtained from the ASTER BBE data. The plots in 'Earth scene' represent each pixel with corresponding Lambertian and temperature properties. Detailed settings of the DART model for the scene simulations can be found in Table 1.

To obtain a suitable tradeoff between the computation cost of DART and the main spectral range in TIR remote sensing, a spectral width of 8–14 μm was chosen. This spectral range was divided into 60 bands with 0.1 μm spectral width, and then the broadband tool was used to integrate radiance results from these bands into 8–14 μm broadband radiance images [W/($m^2 \cdot sr$)] with different viewing perspectives. The number of virtual directions was 720 (20 × 36) in the hemispherical space and the division of VZA and VAA followed Eq. (14). Finally, the directional radiance of DART-simulated projected images (30 m resolution) was used to calculate the radiance at the 1-km pixel assuming that the pixel is a blackbody.

In order to revise the spectral mismatch between the simulated radiance by DART (8 to 14 μm) and that from TLRM (within 4–100 μm), a regression function was generated through the simulation dataset using
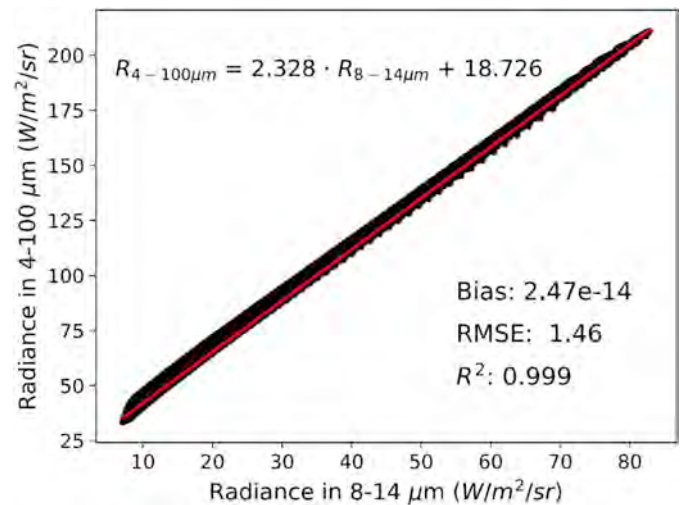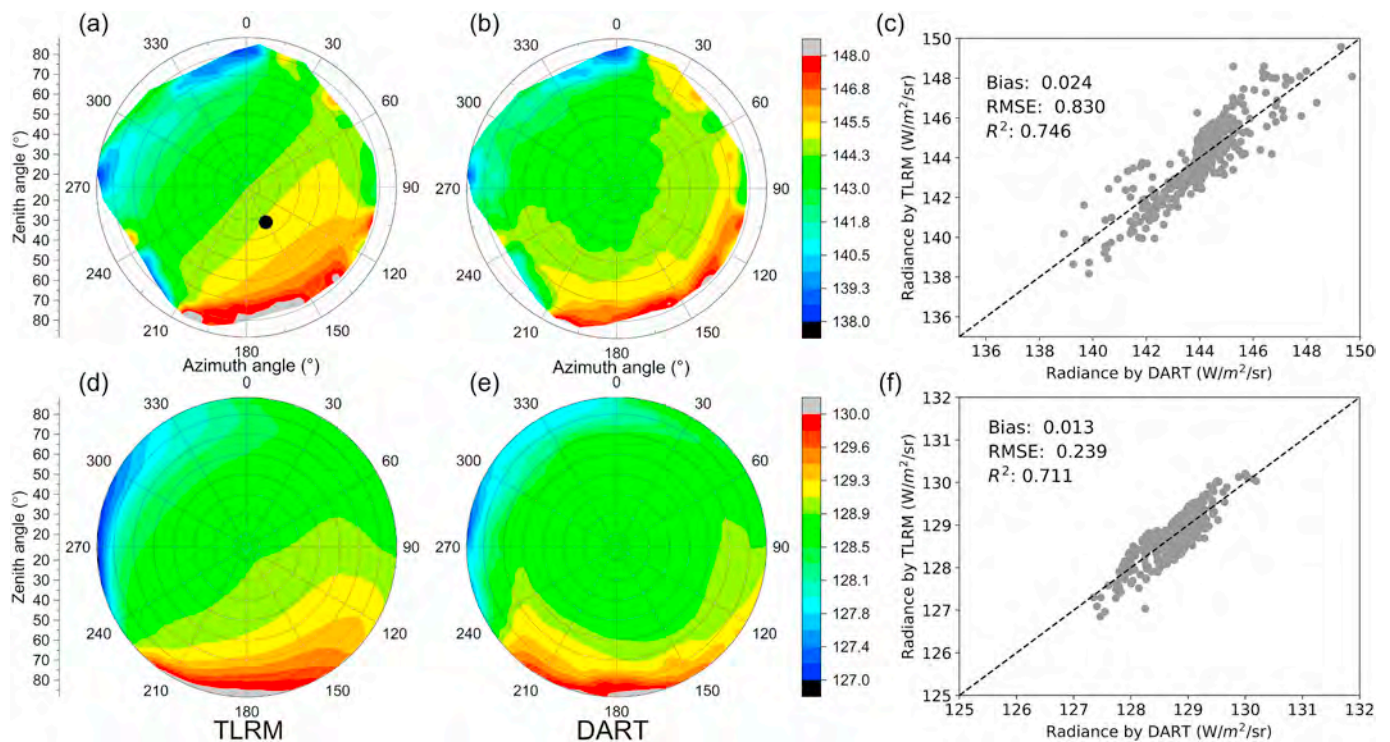
Fig. 5. Radiance values for a 1-km pixel with variable viewing zenith (0°-90°) and azimuth (0°-360°) angles in the hemispheric space. (a) Valley and (d) peak scenes derived from radiance images simulated by the topographic longwave radiation model (TLRM). (b) Valley and (e) peak scenes derived from projected radiance images simulated by the Discrete Anisotropic Radiative Transfer (DART) model. Blank areas in polar plots are due to obstruction by surrounding terrain from some viewing angles. The black dot in (a) denotes the solar position. (c) and (f) Scatter plots between the TLRM and DART models for valley and peak zones, respectively. The dashed line represents the 1:1 line.

2019b). The TLRM (Fig. 5a and d) generated wider and more significant hotspot areas than did the DART model (Fig. 5b and e) in the southeast direction for a solar zenith angle of 26.19° and azimuth angle of 147.89°. Although radiance anisotropy using the DART model was more intricate, high consistency was expected in major low- and high-value areas for the valley scene. Three low-value areas [radiance < 140 W/$(m^2 \cdot sr)$] in the north, west, and southwest directions had high accordance with both the TLRM and DART (Fig. 5a and b). High-value areas from the northeast to south directions with higher VZA also showed great agreement. The peak scene shows similar features with weaker directionality owing to more limited variations in radiance (Fig. 5d and e). This comparison confirms that TLRM is able to capture the anisotropy patterns of radiance in the hemispheric space.

A linear regression was performed to revise the residual discrepancy between the DART model and TLRM after the spectral bandwidth correction (see Section 4). For the valley scene, $Rad_{TLRM} = 1.203 Rad_{DART} - 1.814$, where Rad_{DART} is the radiance simulated by DART and Rad_{TLRM} is the radiance calculated by TLRM; for the peak scene, $Rad_{TLRM} = 1.057 Rad_{DART} + 1.993$. These two linear regressions are similar, indicating relatively good reliability of the simulations. Thus, after revisions by the linear regression models, their biases were found to be 0.024 and 0.013 (Fig. 5c and f, respectively). The RMSE and R^2 were 0.830 W/$(m^2 \cdot sr)$ and 0.746 for the valley scene, and 0.239 W/$(m^2 \cdot sr)$ and 0.711 for the peak scene, respectively.

Radiance profiles at and perpendicular to the solar principal plane according to the solar azimuth angle are presented in Fig. 6. At the solar principal plane, the radiance values from both TLRM and DART exhibited strong anisotropic characteristics for both valley and peak scenes. The radiance values increased from the northwest (327.89°) to

southeast (147.89°) directions with larger variations at larger VZA. TLRM radiance values showed stronger magnitudes than those of DART as the radiance values simulated by DART saw almost no changes within ± 50° (Fig. 6a and c). Furthermore, weak anisotropy of radiance perpendicular to the solar principal plane was apparent (Fig. 6b and d). This suggests that solar position is an important factor in controlling the hemispheric distributions and magnitude of thermal anisotropy. Note that at larger VZA (usually > 60°), the TLRM and DART models both generated strongly drifting radiance values. The two models showed opposite trends for the scenes perpendicular to the solar principal plane (Fig. 6b and d). In addition, many outlier samples were deviated from the overall trend in cases except for the peak scene in the solar principal plane (Fig. 6c). In general, the TLRM showed relatively good performance compared with the DART model.

5.2. Comparisons of TLRM with existing methods

Eq. (3) was used to topographically correct the MODIS-derived SDLR, both of which are illustrated in Fig. 7. The plain region, at a lower altitude, had higher SDLR values than the mountainous areas. The SDLR decreased with elevation and was mainly between 160 and 330 W/m^2. SDLR in plain areas tended to be similar, with values > 300 W/m^2. Land cover in plain areas was the main factor causing the SDLR differences. Topography induces large diversity in complex terrains, and TDLR values have greater spatial variations from peaks to valleys. The difference values between these two products are from 25 to −75 W/m^2 (Fig. 7d), and can be less than −60 W/m^2 in valley areas.

The SDLR in deep valleys originates from two sources: 1) the atmosphere above the valley, and 2) relatively warmer adjacent
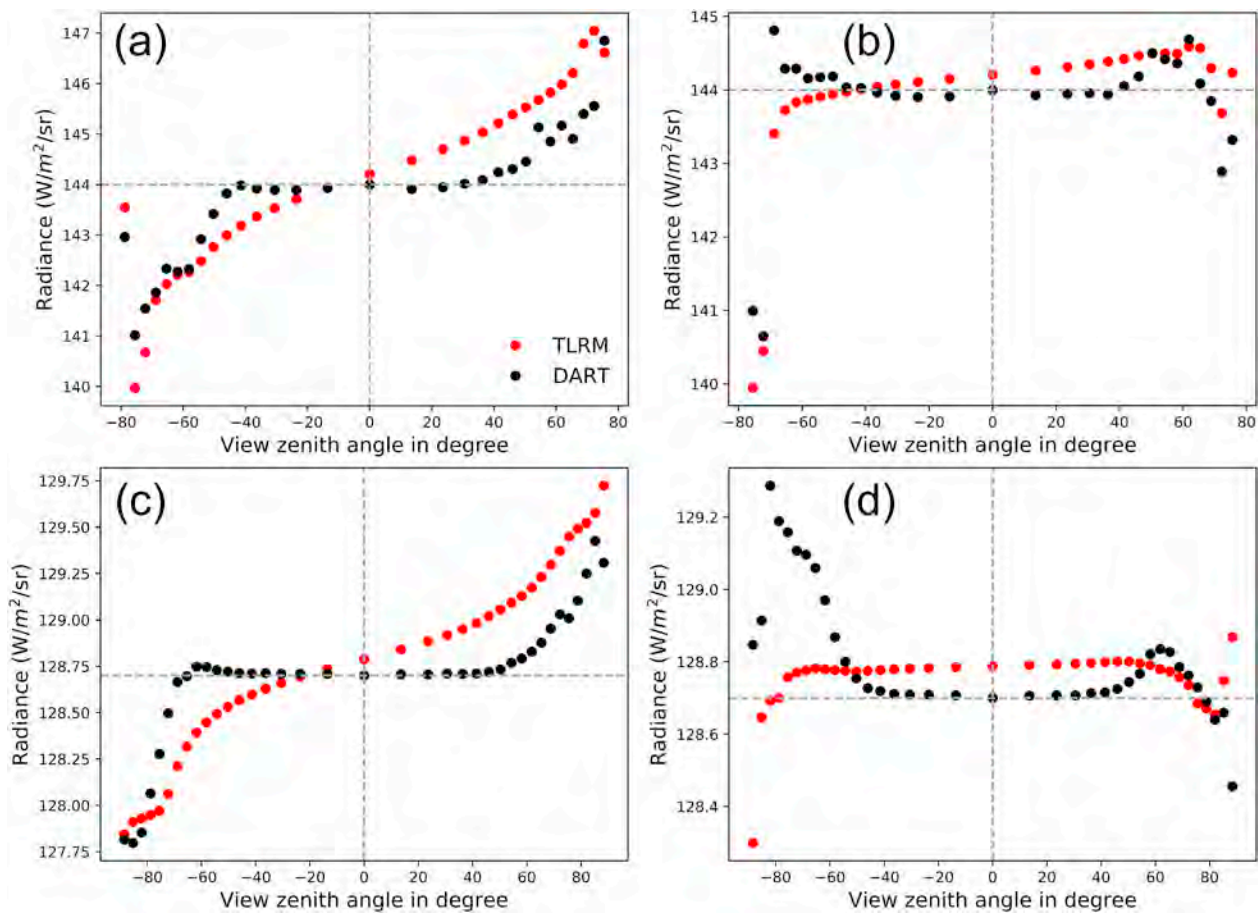
Fig. 6. Radiance profiles derived from the topographic longwave radiation model (TLRM) and Discrete Anisotropic Radiative Transfer (DART) model extracted from the same data presented in Fig. 5. (a) Valley scene at the solar principal plane. (b) Valley scene perpendicular to the solar principal plane. (c) Peak scene in the solar principal plane. (d) Peak scene perpendicular to the solar principal plane.

topographic surfaces. Moreover, warmer mountains have a greater impact on SDLR than cold atmosphere under clear sky conditions (Matzinger et al., 2003). Therefore, the intensities of SDLR depend on the relative proportions of land surface and sky seen within the observation hemisphere. When the topographic effect is considered, valleys can receive more longwave radiation from adjacent terrain and show a higher SDLR.

In addition, different retrieval methods of SULR were compared, including the artificial neural network (ANN)-based direct estimation method (ADM) (Jiao et al., 2015), the directional upward longwave radiation (DULR) model based on Eq. (12), and the proposed HULR model. The results at the 1-km MODIS scale using ASTER data and MODIS SDLR are shown in Fig. 8. The range of SULR was set at 300 to 600 W/m^2 for consistent visualization, and the SULR derived from the ADM method had a smoother transition around adjacent pixels. Both presented similar spatial distributions of SULR for the plains and mountains. In high altitude regions, the SULR was very low, while the plains and valleys had much higher values. Moreover, significant differences in SULR for the plain region reflect the varying LST and emissivity values from different land covers.

To demonstrate the relative biases of different estimation models, the HULR values were treated as references; the difference maps and histograms are presented in Fig. 9. Note that some outliers occur along the boundaries of the study area; these are caused by the effects of invalid values outside of the boundaries. The results indicate that these

methods generate lower biases of SULR in plain regions than in high relief terrain. Compared with the baseline of HULR, the ADM-based SULR, with a mean bias of 11.41 W/m^2 and standard deviation (STD) of 7.30 W/m^2, had higher variation than the DULR, with a mean bias of 5.99 W/m^2 and STD of 4.08 W/m^2, (Fig. 9c and d).

The large altitude variations for valleys and peaks caused significant biases relative to the plain regions. Topography changes the observation geometry and the surface area of a single pixel, and thus affects the proportions of SLR received by a sensor from the atmosphere and from the surrounding terrain. Moreover, the terrain has a significant impact on LST and air temperature; for instance, terrain shadow and different heating magnitudes by solar radiation for tilted surfaces with different slopes and aspects. Therefore, the impact of terrain on SLR estimation cannot be neglected in high relief regions.

Finally, based on the above models, SNLR was estimated as the difference between MODIS SDLR and ADM SULR. The TNLR is the difference between the TDLR and HULR, which was used as the baseline. SNLR is the loss of SLR and is generally negative; that is, SULR is generally greater than SDLR. SNLR reflects the combined effects among the atmospheric states and surface properties (e.g., surface temperature and emissivity), and TDLR is further incorporated for the terrain effect. In Fig. 10, the SNLR ranges approximately -140 to -245 W/m^2, and TNLR is from approximately -75 W/m^2 to -260 W/m^2, which illustrates the net loss of longwave radiant energy from the land surface. More longwave radiation is emitted into the atmosphere in the plain
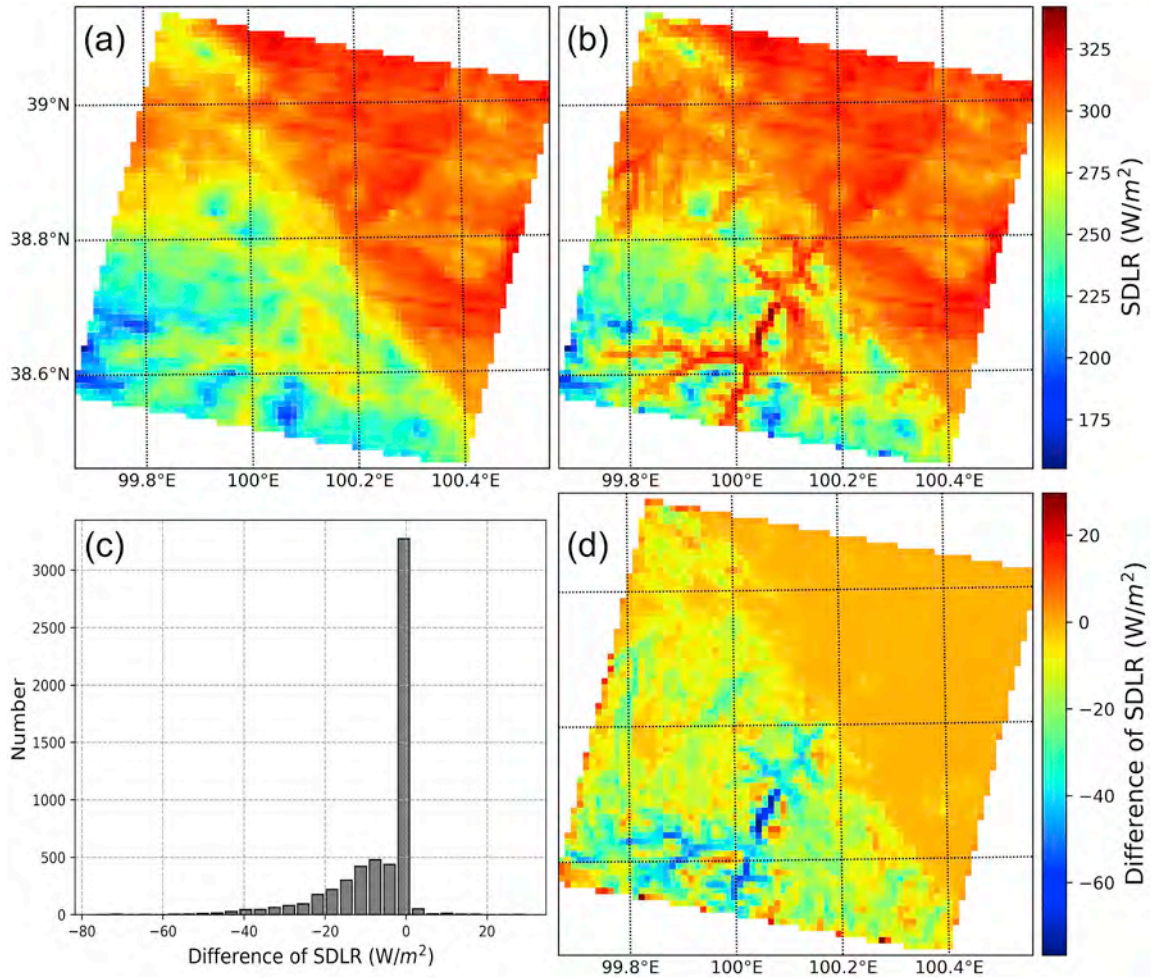
Fig. 7. Comparison of surface downward longwave radiation (SDLR) in the study area (1-km grid) before and after terrain correction. (a) Moderate Resolution Imaging Spectroradiometer (MODIS) derived SDLR. (b) Terrain-corrected SDLR. (c) Difference histogram of SDLR values before and after terrain correction, and (d) difference map corresponding to (c).

areas, which can heat the near-surface atmosphere and hence intensify local heat waves. Valleys can retain more longwave radiation because of the enhanced terrain radiation and limited portion of visible sky (i.e., smaller SVF). SDLR was relatively uniform in the plain areas, and the variance in SNLR was mainly affected by SULR, which showed obvious diversity among land surface covers, such as the significant differences between farmland and desert regions. Their discrepancy ranged between 50 and -130 W/m^2 with obvious negative biases mainly occurring in the valleys (Fig. 10d). The mean bias and STD were -20.28 and 13.66 W/m^2, respectively, indicating that the TNLR was larger than the SNLR in most areas.

5.3. Impact of atmosphere on LRST

If the effects of atmospheric absorption and emission of longwave radiation are considered between points M and P (Fig. 3c), adjacent terrain radiation becomes more complex. Eq. (16) should be modified to include the influence of the atmosphere, as follows:

$$L_{adj} = \Theta_{M \to P} \left[\frac{\tau}{\pi} [\varepsilon_P \sigma T_P^4 + (1 - \varepsilon_P)(E_P^\downarrow + E_T)] + L_P \right] \tag{17}$$

where τ is the transmittance of the atmosphere between points M and P,

and L_P is the path radiance between them. To analyze the radiation contribution from surrounding terrain and its influencing factors, sensitivity analyses were conducted based on MODTRAN simulations and the above formula.

Fig. 11a shows that radiance values received by the observation point change with observation distance under different temperature conditions at the target point. The observation point receives only the atmospheric path radiation when the LST of the target point is set to 0.01 K. With an increase in observation distance, the radiation contribution from the target point (i.e., surrounding terrain) gradually decreases, while the radiation contribution of the atmosphere increases. The surface temperature of a target point at 293.15 K is similar to an air temperature of 294.2 K, and thus the radiance received is almost independent of the observation distance. In summer, air temperature is generally lower than surface temperature; hence, the observed radiance gradually decreases with increasing distance. In contrast, the observed radiance progressively increases with increasing distance during the winter because of the higher air temperature, especially for snow-covered surfaces. In all four cases, with the increase in distance, the observed radiance values reached the same level, one that consisted mostly of the atmospheric path radiation. Therefore, the temperature difference between the target and the atmosphere is an important factor
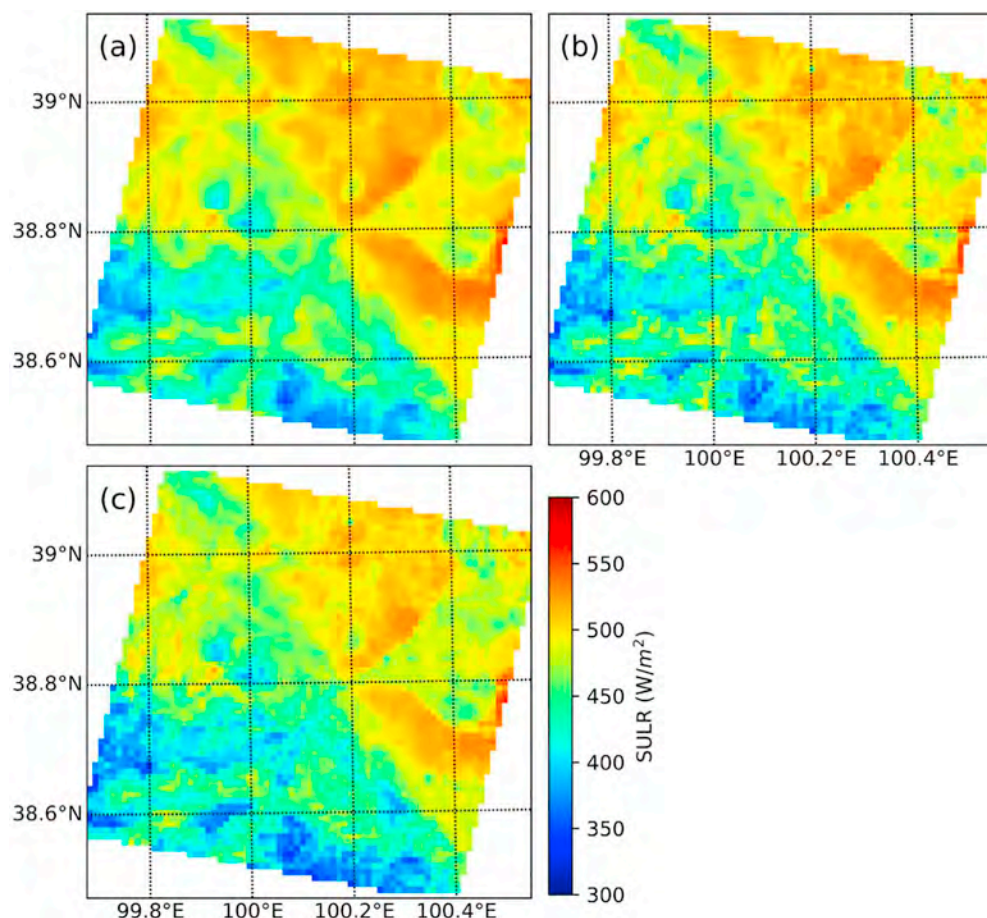
Fig. 8. Moderate Resolution Imaging Spectroradiometer (MODIS) 1-km surface upward longwave radiation (SULR). Results derived using the (a) artificial neural networks (ANN)-based direct estimation method (ADM), (b) directional upward longwave radiation (DULR) model and (c) hemispherical upward longwave radiation (HULR) model.

in estimating LSTR.

Fig. 11b presents the curves of atmospheric transmittance according to six atmosphere types in the MODTRAN model. With increasing distance, both the transmittance of the atmosphere and the radiation contribution of the target point to the observation point are reduced. This explains why values of observed radiance become relatively uniform when the distance is sufficiently large (Fig. 11a). One of the dominant factors affecting atmospheric transmittance in TIR wavelengths is total column water content. The Tropical atmosphere has a high water vapor content, which leads to minimal atmospheric transmittance; while Sub-Arctic Winter atmosphere has maximal transmittance due to the very low humidity. Therefore, the water vapor content is another important factor affecting radiation from the surrounding terrain. At the same time, atmospheric transmittance also represents the contribution proportion of the terrain radiation at a given distance. For example, the atmospheric transmittance is only approximately 15% at a distance of 3 km for the Mid-Latitude Summer atmosphere, while this value is ~30% for Mid-Latitude Winter atmosphere.

In summary, the difference between the temperature of the surrounding terrain and air temperature, and the water vapor content are two major factors that affect the contribution of adjacent terrain radiation. The atmospheric path radiation should be taken into account when calculating the LRST. However, air temperature and humidity are rarely obtained at the pixel scale. The MOD07 product has the highest spatial-resolution among atmospheric profile products with a resolution of 5 km. Nevertheless, this resolution is not fine enough for a 30-m subpixel cell within a 1-km pixel. The interpolation of MOD07 data to

30-m resolution can cause artificial atmospheric status. To simplify this calculation, it is better to calculate terrain radiation using a certain search distance. With an increase in the water vapor content, the search radius becomes smaller. However, when the temperature difference is large, bias error induced by this approximate calculation is significant. Unless the air temperature is equal to the target temperature, a longer search radius will cause a larger bias error when ignoring the influence of the atmosphere.

6. Conclusions

In this study, we developed the TLRM to estimate longwave radiation components for high relief terrain using ASTER and MODIS data. The TLRM considers terrain effects, adjacent terrain radiation and angular effects of thermal radiation induced by the terrain in the azimuth direction. Grid and subgrid-level radiation parameterization schemes allow remote sensing images to be used to calculate SLR components by considering any fine-resolution topography without losing the computational performance. TLRM calculates surface longwave flux at the pixel scale based on ASTER DEM, LST, and BBE data with full spatial resolution. Therefore, it does not require problematic calculations of average terrain properties such as the slope angle and SVF.

DART simulations in the thermal domain were used to validate TLRM and analyze terrain effects on the surface upward longwave radiance in the hemispherical space over two typical geomorphic regions. MODTRAN simulations were performed to correct the spectral mismatch between DART simulations and TLRM outputs, and then the
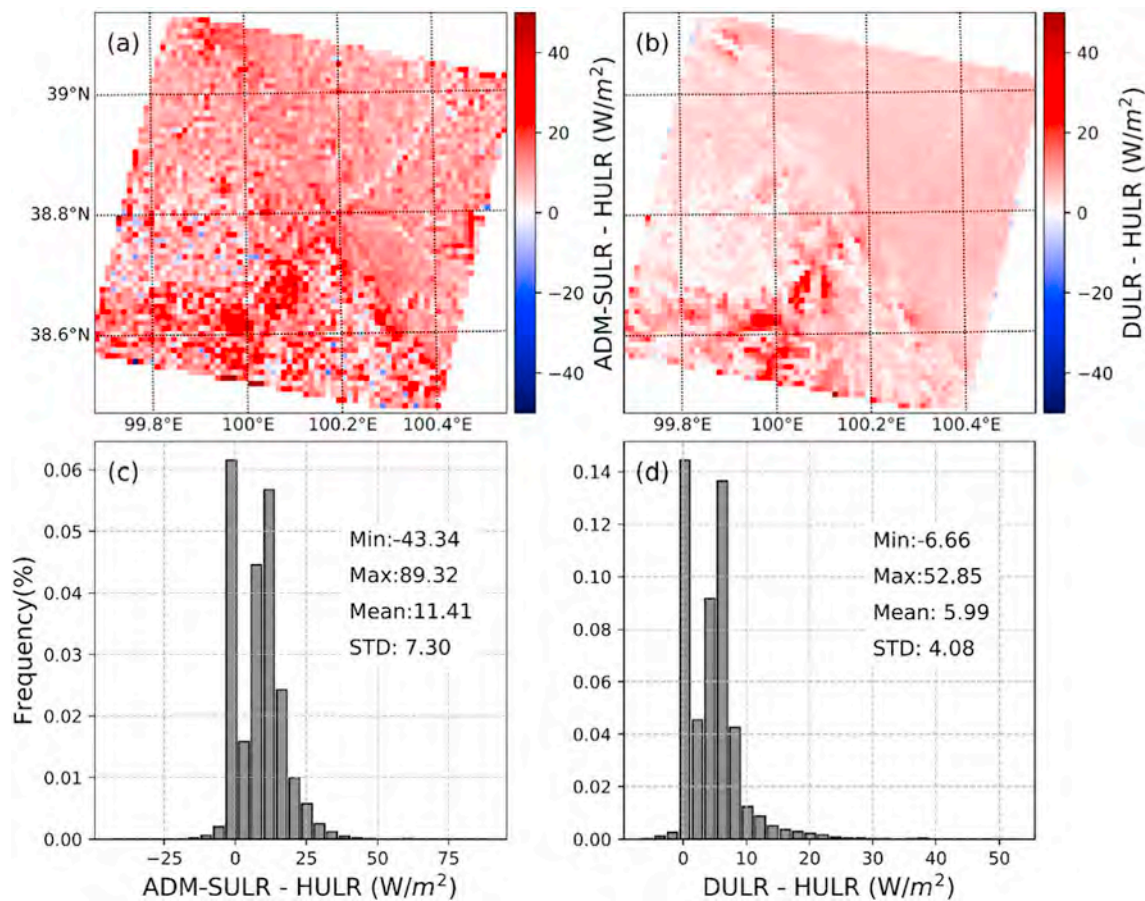
Fig. 9. Difference for results obtained using different models. (a) Difference map between Moderate Resolution Imaging Spectroradiometer (MODIS) surface upward longwave radiation (SULR) derived from the artificial neural networks (ANN)-based direct estimation method (ADM) and from the hemispherical upward longwave radiation (HULR) model. (b) Difference map between SULR derived from directional upward longwave radiation (DULR) model and from the HULR model. (c) Difference histogram corresponding to (a). (d) Difference histogram corresponding to (b).

residual discrepancy was corrected by linear regression. The preliminary validation illustrates good agreement between the DART simulation and TLRM results, which confirms that TLRM is able to capture the anisotropy patterns of surface upward longwave radiance. Comparative analysis of three SLR components revealed that the terrain effects on SLR cannot be ignored. Topography has a significant impact on the surface thermal environment through terrain shadowing and different heating magnitudes of solar radiation for tilted surfaces with different orientations. It also changes the observation geometry and surface area of a single pixel and thus affects the proportion of SLR from the atmosphere and surrounding terrain that is received by a sensor. Moreover, the atmospheric path radiation should be taken into account when calculating terrain radiation. The differences between the target temperature of the surrounding terrain and the air temperature, and water vapor content are two dominant factors that affect the contribution of LRST. However, air temperature and humidity are rarely obtained at the pixel scale and a simplified approach is always used in the calculation of LRST.

A rapid and accurate operational forward TLRM is required in the calculation of SLR for high relief terrains. Owing to the complexity of SLR and the influence of mountainous terrain and local microclimates, to date, SLR products derived from airborne or satellite sensors related to terrain effects have not been accessible. Thus, modeling SLR

components in complex terrains continues to be a challenge and remains a subject of research interest. As an exploration of directional thermal radiation modeling, the TLRM is helpful in understanding the comprehensive influences of surface heterogeneity and topographic effects. The results of this study will enable models of Earth-atmosphere processes in high relief regions to be more accurate and reasonable. This in turn will improve simulations and predictions of, among others, biophysical parameters of hydrology, ecology, and agriculture, and offer an improved understanding of formation mechanisms and changes in regional climate. However, considerable effort is still needed to improve SLR models with respect to terrain effects. In future work, the combination of the DART model with detailed ground measurements will allow for a more robust validation of our model by quantifying the effects of terrain on SLR.

Declaration of competing interest

The authors declare that they have no known competing financial interests or personal relationships that could have appeared to influence the work reported in this paper.
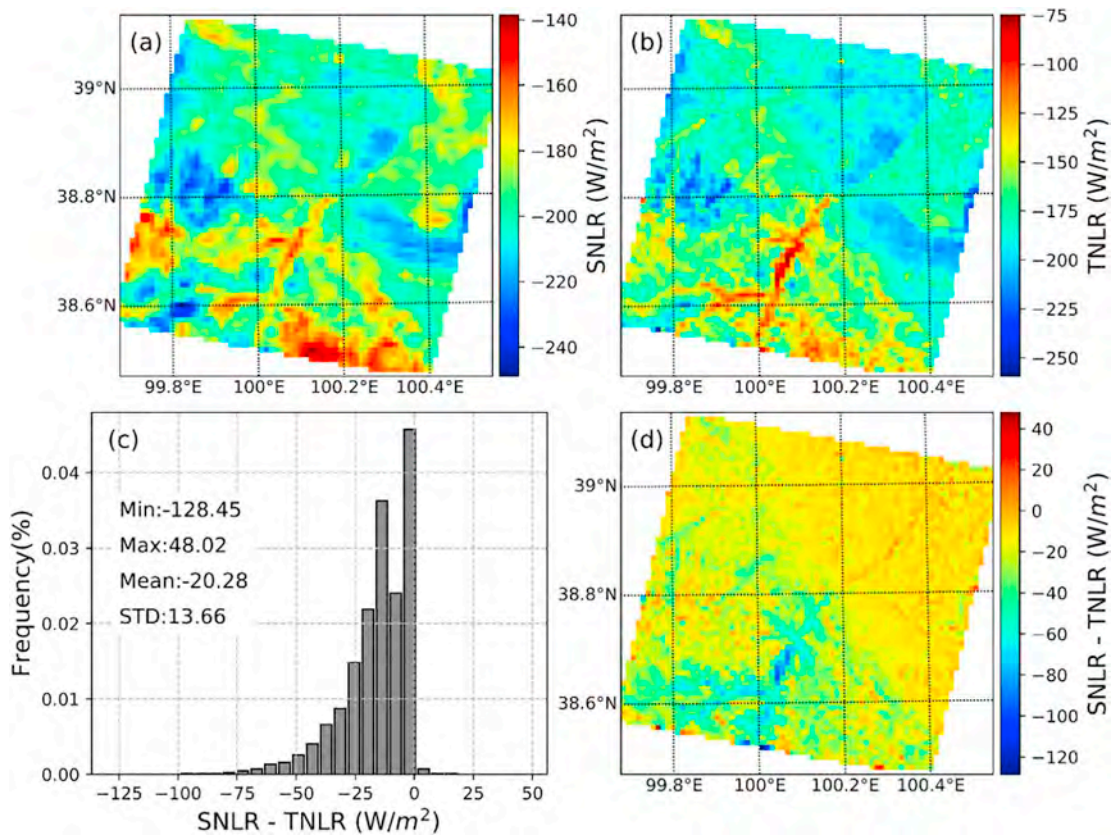
Fig. 10. Comparison of net longwave radiation at the 1-km spatial scale before and after terrain correction. (a) Surface net longwave radiation (SNLR) calculated using Moderate Resolution Imaging Spectroradiometer (MODIS) surface downward longwave radiation (SDLR) and the artificial neural networks (ANN)-based direct estimation method (ADM) surface upward longwave radiation (SULR). (b) Terrain-corrected net longwave radiation (TNLR) using terrain-corrected downward longwave radiation (TDLR) and hemispherical upward longwave radiation (HULR). (c) Difference histogram between SNLR and TNLR and (d) the corresponding difference map.
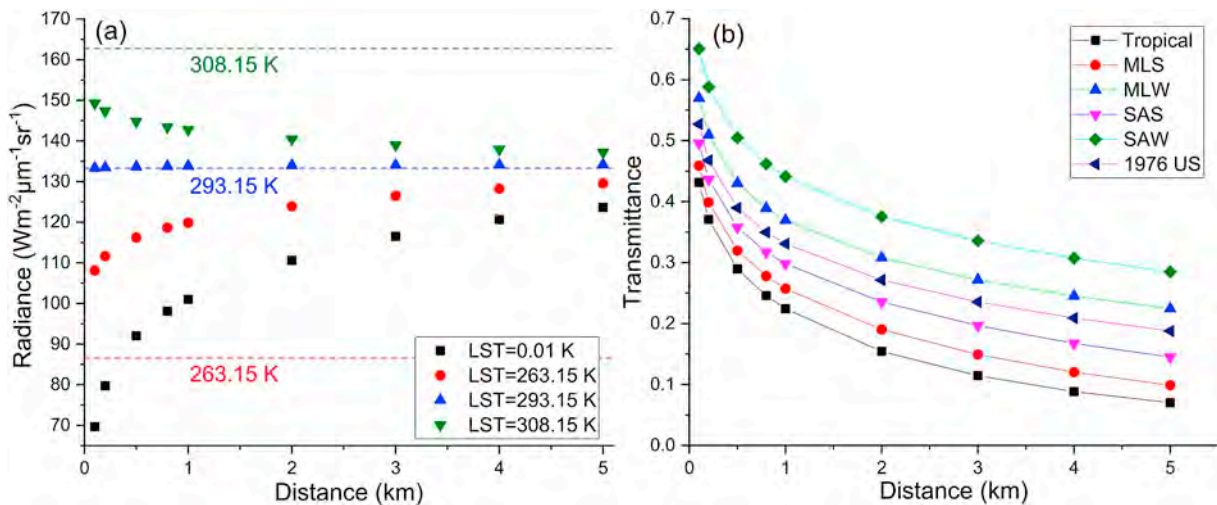

Fig. 11. Radiance and atmospheric transmittance as function of distance. (a) Observed radiance in a horizontal path with varying distance, assuming a Mid-Latitude Summer atmosphere, a surface elevation of 0 km, an air temperature of 294.2 K, and a blackbody surface. The dashed lines indicate radiance values for the blackbody at target points with different temperatures. (b) Atmospheric transmittance curves in a horizontal path at sea level with varying distance. MLS is the Mid-Latitude Summer atmosphere, MLW is the Mid-Latitude Winter atmosphere, SAS is the Sub-Arctic Summer atmosphere, and SAW is the Sub-Arctic Winter atmosphere.

Acknowledgments

Appendix A. List of acronyms

Acronym	Phrase
3D	three-dimensional
ADM	ANN-based direct estimation method
ANN	artificial neural networks
ASTER	Advanced Spaceborne Thermal Emission and Reflection Radiometer
BBE	broadband emissivity
BT	brightness temperature
DART	Discrete Anisotropic Radiative Transfer
DEM	digital elevation model
DULR	directional upward longwave radiation
GDEM	Global Digital Elevation Model
HULR	hemispherical upward longwave radiation
LRST	longwave radiation from surrounding terrain
LST	land surface temperature
MODIS	Moderate Resolution Imaging Spectroradiometer
MODTRAN	MODerate resolution atmospheric TRANsmission
RMSE	root mean square error
SDLR	surface downward longwave radiation
SLR	surface longwave radiation
SNLR	surface net longwave radiation
STD	standard deviation
SULR	surface upward longwave radiation
SVF	sky view factor
TDLR	terrain-corrected downward longwave radiation
TES	Temperature-Emissivity Separation
TIR	thermal infrared
TLRM	topographic longwave radiation model
TNLR	terrain-corrected net longwave radiation
UTM	Universal Transverse Mercator
VAA	view azimuth angle
VZA	view zenith angle

References

Barnes, W.L., Pagano, T.S., Salomonson, V.V., 1998. Prelaunch characteristics of the Moderate Resolution Imaging Spectroradiometer (MODIS) on EOS-AM1. IEEE Trans. Geosci. Remote Sens. 36, 1088–1100.

Berk, A., Anderson, G.P., Acharya, P.K., Bernstein, L.S., Muratov, L., Lee, J., Fox, M., Adler-Golden, S.M., Chetwynd, J.J.H., Hoke, M.L., Lockwood, R.B., Gardner, J.A., Cooley, T.W., Borel, C.C., Lewis, P.E., Shettle, E.P., 2006. MODTRAN5: 2006 update. In: Algorithms and Technologies for Multispectral, Hyperspectral, and Ultraspectral Imagery XII. Orlando (Kissimmee), FL Proc. SPIE 6233pp. 62331F.

Dozier, J., Frew, J., 1990. Rapid calculation of terrain parameters for radiation modeling from digital elevation data. IEEE Trans. Geosci. Remote Sens. 28, 963–969.

Fiddes, J., Gruber, S., 2014. TopoSCALE v.1.0: downscaling gridded climate data in complex terrain. Geosci. Model Dev. 7, 387–405.

Fontanilles, G., Briottet, X., Fabre, S., Trémas, T., 2008. Thermal infrared radiance simulation with aggregation modeling (TITAN): an infrared radiative transfer model for heterogeneous three-dimensional surface—application over urban areas. Appl. Opt. 47, 5799–5810.

Fontanilles, G., Briottet, X., Fabre, S., Lefebvre, S., Vandenhaute, P.-F., 2010. Aggregation process of optical properties and temperature over heterogeneous surfaces in infrared domain. Appl. Opt. 49, 4655–4669.

Francois, C., Ottle, C., Prevot, L., 1997. Analytical parameterization of canopy directional emissivity and directional radiance in the thermal infrared. Application on the retrieval of soil and foliage temperatures using two directional measurements. Int. J. Remote Sens. 18, 2587–2621.

Gastellu-Etchegorry, J.P., Demarez, V., Pinel, V., Zagolski, F., 1996. Modeling radiative transfer in heterogeneous 3-D vegetation canopies. Remote Sens. Environ. 58, 131–156.

Gastellu-Etchegorry, J.-P., Yin, T., Lauret, N., Cajgfinger, T., Gregoire, T., Grau, E., Feret, J.-B., Lopes, M., Guilleux, J., Dedieu, G., Malenovský, Z., Cook, B.D., Morton, D., Rubio, J., Durrieu, S., Cazanave, G., Martin, E., Ristorcelli, T., 2015. Discrete anisotropic radiative transfer (DART 5) for modeling airborne and satellite spectroradiometer and LIDAR acquisitions of natural and urban landscapes. Remote Sens. 7, 1667–1701.

Gillespie, A., Rokugawa, S., Matsunaga, T., Cothern, J.S., Hook, S., Kahle, A.B., 1998. A temperature and emissivity separation algorithm for Advanced Spaceborne Thermal Emission and Reflection Radiometer (ASTER) images. IEEE Trans. Geosci. Remote Sens. 36, 1113–1126.

Gratton, D.J., Howarth, P.J., Marceau, D.J., 1993. Using Landsat-5 thematic mapper and digital elevation data to determine the net radiation field of a mountain glacier. Remote Sens. Environ. 43, 315–331.

Hoch, S.W., Whiteman, C.D., 2010. Topographic effects on the surface radiation balance in and around Arizona's Meteor Crater. J. Appl. Meteorol. Climatol. 49, 1114–1128.

Hock, R., Holmgren, B., 2005. A distributed surface energy-balance model for complex topography and its application to Storglaciaren, Sweden. J. Glaciol. 51, 25–36.

Jiao, Z., Yan, G., Zhao, J., Wang, T., Chen, L., 2015. Estimation of surface upward longwave radiation from MODIS and VIIRS clear-sky data in the Tibetan Plateau. Remote Sens. Environ. 162, 221–237.

Jiao, Z.-H., Ren, H., Mu, X., Zhao, J., Wang, T., Dong, J., 2019a. Evaluation of four sky view factor algorithms using digital surface and elevation model data. Earth Space Sci. 6, 222–237.

Jiao, Z., Yan, G., Wang, T., Mu, X., Zhao, J., 2019b. Modeling of land surface thermal anisotropy based on directional and equivalent brightness temperatures over complex terrain. IEEE J. Sel. Top. Appl. Earth Obs. Remote Sens. 12, 410–423.

Kimes, D.S., Kirchner, J.A., 1983. Directional radiometric measurements of row-crop temperatures. Int. J. Remote Sens. 4, 299–311.

Labed, J., Stoll, M.P., 1991. Spatial variability of land surface emissivity in the thermal infrared band: spectral signature and effective surface temperature. Remote Sens. Environ. 38, 1–17.

Lagouarde, J.P., Kerr, Y.H., Brunet, Y., 1995. An experimental study of angular effects on surface temperature for various plant canopies and bare soils. Agric. For. Meteorol. 77, 167–190.

Lagouarde, J.-P., Moreau, P., Irvine, M., Bonnefond, J.-M., Voogt, J.A., Solliec, F., 2004. Airborne experimental measurements of the angular variations in surface temperature over urban areas: case study of Marseille (France). Remote Sens. Environ. 93,

443–462.

Lai, Y.-J., Chou, M.-D., Lin, P.-H., 2010. Parameterization of topographic effect on surface solar radiation. J. Geophys. Res. Atmos. 115, D01104.

Lee, W.-L., Liou, K.N., Wang, C., 2013. Impact of 3-D topography on surface radiation budget over the Tibetan Plateau. Theor. Appl. Climatol. 113, 95–103.

Li, X., Wang, J., 1999. The definition of effective emissivity of land surface at the scale of remote sensing pixels. Chin. Sci. Bull. 44, 2154–2158.

Li, X., Strahler, A.H., Friedl, M.A., 1999a. A conceptual model for effective directional emissivity from nonisothermal surfaces. IEEE Trans. Geosci. Remote Sens. 37, 2508–2517.

Li, X., Wang, J., Strahler, A.H., 1999b. Scale effect of Planck's law over nonisothermal blackbody surface. Sci. China, Ser. E: Technol. Sci. 42, 652–656.

Liou, K.N., Lee, W.-L., Hall, A., 2007. Radiative transfer in mountains: application to the Tibetan Plateau. Geophys. Res. Lett. 34, L23809.

Lipton, A.E., Ward, J.M., 1997. Satellite-view biases in retrieved surface temperatures in mountain areas. Remote Sens. Environ. 60, 92–100.

Liu, Y., Hiyama, T., Yamaguchi, Y., 2006. Scaling of land surface temperature using satellite data: a case examination on ASTER and MODIS products over a heterogeneous terrain area. Remote Sens. Environ. 105, 115–128.

Manners, J., Vosper, S.B., Roberts, N., 2012. Radiative transfer over resolved topographic features for high-resolution weather prediction. Q. J. R. Meteorol. Soc. 138, 720–733.

Matzinger, N., Andretta, M., Gorsel, E.V., Vogt, R., Ohmura, A., Rotach, M.W., 2003. Surface radiation budget in an Alpine valley. Q. J. R. Meteorol. Soc. 129, 877–895.

Minnis, P., Gambheer, A.V., Doelling, D.R., 2004. Azimuthal anisotropy of longwave and infrared window radiances from the Clouds and the Earth's Radiant Energy System on the Tropical Rainfall Measuring Mission and Terra satellites. J. Geophys. Res. Atmos. 109, D08202.

Müller, M.D., Scherer, D., 2005. A grid- and subgrid-scale radiation parameterization of topographic effects for Mesoscale weather forecast models. Mon. Weather Rev. 133, 1431–1442.

Ogawa, K., Schmugge, T., 2004. Mapping surface broadband emissivity of the Sahara Desert using ASTER and MODIS data. Earth Interact. 8, 1–14.

Ogawa, K., Schmugge, T., Jacob, F., French, A., 2002. Estimation of broadband land surface emissivity from multi-spectral thermal infrared remote sensing. Agronomie 22, 695–696.

Ogawa, K., Schmugge, T., Jacob, F., French, A., 2003. Estimation of land surface window (8–12 μm) emissivity from multi-spectral thermal infrared remote sensing — a case study in a part of Sahara Desert. Geophys. Res. Lett. 30, 1067.

Olyphant, G.A., 1986a. The components of incoming radiation within a mid-latitude alpine watershed during the snowmelt season. Arct. Alp. Res. 18, 163–169.

Olyphant, G.A., 1986b. Longwave radiation in mountainous areas and its influence on the energy balance of alpine snowfields. Water Resour. Res. 22, 62–66.

Plüss, C., Ohmura, A., 1997. Longwave radiation on snow-covered mountainous surfaces. J. Appl. Meteorol. 36, 818–824.

Proy, C., Tanré, D., Deschamps, P.Y., 1989. Evaluation of topographic effects in remotely sensed data. Remote Sens. Environ. 30, 21–32.

Ren, H., Yan, G., Liu, R., Nerry, F., Li, Z.-L., Hu, R., 2013a. Impact of sensor footprint on measurement of directional brightness temperature of row crop canopies. Remote Sens. Environ. 134, 135–151.

Ren, H.Z., Liang, S.L., Yan, G.J., Cheng, J., 2013b. Empirical algorithms to map global broadband emissivities over vegetated surfaces. IEEE Trans. Geosci. Remote Sens. 51,

2619–2631.

Senkova, A.V., Rontu, L., SavijÄRvi, H., 2007. Parametrization of orographic effects on surface radiation in HIRLAM. Tellus A 59, 279–291.

Sicart, J.E., Pomeroy, J.W., Essery, R.L.H., Bewley, D., 2006. Incoming longwave radiation to melting snow: observations, sensitivity and estimation in northern environments. Hydrol. Process. 20, 3697–3708.

Sobrino, J.A., Jimenez-Munoz, J.C., Balick, L., Gillespie, A.R., Sabol, D.A., Gustafson, W.T., 2007. Accuracy of ASTER level-2 thermal-infrared standard products of an agricultural area in Spain. Remote Sens. Environ. 106, 146–153.

Sobrino, J.A., Mattar, C., Gastellu-Etchegorry, J.P., Jiménez-Muñoz, J.C., Grau, E., 2011. Evaluation of the DART 3D model in the thermal domain using satellite/airborne imagery and ground-based measurements. Int. J. Remote Sens. 32, 7453–7477.

Sugawara, H., Takamura, T., 2006. Longwave radiation flux from an urban canopy: evaluation via measurements of directional radiometric temperature. Remote Sens. Environ. 104, 226–237.

Tachikawa, T., Kaku, M., Iwasaki, A., Gesch, D.B., Oimoen, M.J., Zhang, Z., Danielson, J.J., Krieger, T., Curtis, B., Haase, J., Abrams, M., Carabajal, C., 2011. ASTER Global Digital Elevation Model Version 2 - Summary of Validation Results, 2 ed. USGS Publications Warehouse: NASA.

Voogt, J.A., 2008. Assessment of an urban sensor view model for thermal anisotropy. Remote Sens. Environ. 112, 482–495.

Wang, T., Yan, G., Chen, L., 2012. Consistent retrieval methods to estimate land surface shortwave and longwave radiative flux components under clear-sky conditions. Remote Sens. Environ. 124, 61–71.

Wang, T., Shi, J., Yu, Y., Husi, L., Gao, B., Zhou, W., Ji, D., Zhao, T., Xiong, C., Chen, L., 2018a. Cloudy-sky land surface longwave downward radiation (LWDR) estimation by integrating MODIS and AIRS/AMSU measurements. Remote Sens. Environ. 205, 100–111.

Wang, T., Yan, G., Mu, X., Jiao, Z., Chen, L., Chu, Q., 2018b. Toward operational shortwave radiation modeling and retrieval over rugged terrain. Remote Sens. Environ. 205, 419–433.

Widlowski, J.-L., Mio, C., Disney, M., Adams, J., Andredakis, I., Atzberger, C., Brennan, J., Busetto, L., Chelle, M., Ceccherini, G., Colombo, R., Côté, J.-F., Eenmäe, A., Essery, R., Gastellu-Etchegorry, J.-P., Gobron, N., Grau, E., Haverd, V., Homolová, L., Huang, H., Hunt, L., Kobayashi, H., Koetz, B., Kuusk, A., Kuusk, J., Lang, M., Lewis, P.E., Lovell, J.L., Malenovský, Z., Meroni, M., Morsdorf, F., Mõttus, M., Ni-Meister, W., Pinty, B., Rautiainen, M., Schlerf, M., Somers, B., Stuckens, J., Verstraete, M.M., Yang, W., Zhao, F., Zenone, T., 2015. The fourth phase of the radiative transfer model intercomparison (RAMI) exercise: actual canopy scenarios and conformity testing. Remote Sens. Environ. 169, 418–437.

Wielicki, B.A., Barkstrom, B.R., Harrison, E.F., Lee, R.B., Louis Smith, G., Cooper, J.E., 1996. Clouds and the Earth's Radiant Energy System (CERES): an earth observing system experiment. Bull. Am. Meteorol. Soc. 77, 853–868.

Yan, G., Friedl, M., Li, X., Wang, J., Zhu, C., Strahler, A.H., 2001. Modeling directional effects from nonisothermal land surfaces in wideband thermal infrared measurements. IEEE Trans. Geosci. Remote Sens. 39, 1095–1099.

Yan, G., Wang, T., Jiao, Z., Mu, X., Zhao, J., Chen, L., 2016. Topographic radiation modeling and spatial scaling of clear-sky land surface longwave radiation over rugged terrain. Remote Sens. Environ. 172, 15–27.

Yi, B., Yang, P., Liou, K.-N., Minnis, P., Penner, J.E., 2012. Simulation of the global contrail radiative forcing: a sensitivity analysis. Geophys. Res. Lett. 39, L00F03.